The Gibbs–Thomson effect in magnetron-sputtered austenitic stainless steel films

2007 J. Phys.: Condens. Matter 19 106211

(http://iopscience.iop.org/0953-8984/19/10/106211)

IOP PUBLISHING JOURNAL OF PHYSICS: CONDENSED MATTER

J. Phys.: Condens. Matter **19** (2007) 106211 (19pp) doi:10.1088/0953-8984/19/10/106211

The Gibbs–Thomson effect in magnetron-sputtered austenitic stainless steel films

S Cusenza[1], C Borchers[1], E Carpene[2] and P Schaaf[1]

[1] Universität Göttingen, II Physikalisches Institut, Friedrich-Hund-Platz 1, 37077 Göttingen, Germany
[2] Politecnico di Milano, Dipartimento di Fisica, Piazza Leonardo da Vinci 32, 20133 Milano, Italy

E-mail: pschaaf@uni-goettingen.de

Received 23 October 2006, in final form 29 January 2007
Published 16 February 2007
Online at stacks.iop.org/JPhysCM/19/106211

Abstract

Magnetron sputtering of austenitic stainless steel AISI 316, which has a face-centred cubic structure (γ), leads to films exhibiting a body-centred cubic (α) structure or a mixture of α- and γ-phases. The microstructure of the deposited films was studied by Mössbauer spectroscopy, x-ray diffraction and transmission electron microscopy. With increasing deposition temperature a phase transformation from α- to γ-phase was observed in these films. Instantaneous recording of the electromotive force shows that nickel content and deposition temperature are crucial factors for phase stability and phase formation. In room temperature deposited stainless steel films, the phase transformation after vacuum annealing can be described by the Johnson–Mehl–Avrami kinetic model. These phase transformations in stainless steel films during annealing can be explained with the Gibbs–Thomson effect, where the grain boundary energy raises the Gibbs free energy.

(Some figures in this article are in colour only in the electronic version)

1. Introduction

The austenitic stainless steel family (AISI 304, 310, 316, 330, etc) is known to have a face-centred cubic (fcc) structure (γ-phase) and to be paramagnetic (non-magnetic) at room temperature. In contrast, ferritic stainless steels have a body-centred cubic (bcc) structure (α-phase), which is in general ferromagnetic at room temperature. The magnetic properties of these Fe-based alloys are one of the innumerable interesting aspects of magnetism. In addition, austenitic stainless steels are used as construction materials for many industrial applications (in the food industry, medical industry and construction industry) due to their excellent corrosion resistance. For some applications better wear resistance of this material would be desirable.

From an industrial point of view, it would be interesting to deposit austenitic stainless steel films onto cheaper materials in order to obtain similarly good corrosion resistance

properties. Several deposition techniques have been used to form these stainless steel films, including ion beam sputtering [1–3], magnetron sputtering [4–6], arc discharge [7] and thermal evaporation [8]. One of the first works on this topic was published by Dahlgren [9]. He investigated AISI 304L films that were sputter deposited onto copper substrates at temperatures in the range of 274–1073 K. Samples deposited below 648 K exhibited the α-phase. Samples deposited in the temperature range of 648–773 K showed a mixture of the α- and γ-phase. Above 773 K, the samples appeared in the γ-phase accompanied by an unknown phase. Malavasi *et al* [10] obtained AISI 304 films of α-structure when deposited at room temperature on glass and ion-cleaned austenitic stainless steel substrates and investigated the Gibbs free energy as a function of the grain size. Li *et al* [11] investigated post-vacuum annealing of sputtered AISI 304 layers. After annealing at 973 K, a phase transformation from the metastable α-phase to the γ-phase was observed. This leads to the conclusion that the temperature is a crucial factor for phase formation. Zhang *et al* [12] investigated the magnetic behaviour of sputtered AISI 304 and AISI 330 layers. They mentioned a depletion of Ni content, but this phenomenon has not been further investigated. All previously cited works state that films deposited at room temperature were in the α-phase.

In this paper we report on the structural and magnetic properties of austenitic stainless steel films prepared by rf-magnetron sputtering from an AISI 316 target. The effects of temperature during and after deposition were studied as well as the electrochemical behaviour of the samples, which leads to another important factor for phase stability and formation: the Ni content. Ni is known to be a γ-phase stabilizer. In equilibrium, 8 wt% Ni is sufficient to stabilize the γ-phase in bulk material. As a consequence of this, we performed an accurate composition analysis, where Ni depletion was also found to be the reason of the formation of the α-phase instead of the γ-phase.

2. Experimental details

The films were sputter-deposited with an rf magnetron onto amorphous SiO_2 substrates (oxidized Si(100) wafer) utilizing a commercial AISI 316 (Fe-18Cr-10Ni-3Mo, 1.4401) target. The target–substrate distance was set to 12 cm. The processing parameters were 100 W magnetron power at a constant Ar gas flow during deposition. Several series were done at different gas flows (6–12 sccm). The sputter rate ranged from 1.4–3.4 Å s^{-1}, depending on the processing parameters. The magnetron chamber was evacuated to a base pressure of 10^{-4} Pa before deposition. The AISI 316 target was always pre-sputtered for half an hour. The thickness of the films varied from 190 to 210 nm and was controlled by a quartz microbalance.

Conversion electron Mössbauer spectroscopy (CEMS) was performed at room temperature, employing a ^{57}Co/Rh γ-ray source in constant acceleration mode. The electrons were detected in a CH_4/He flow proportional counter [13, 14]. The spectra were fitted by a field distribution calculated with the Normos code [15] or by superimposing Lorentzian lines with the WinISO fitting tool [16]. Velocity calibration was performed using an α-Fe foil and the isomer shifts are stated relative to the centre of this calibration.

Crystallographic analyses were performed by grazing incidence x-ray diffraction (GIXRD) using a Bruker AXS diffractometer equipped with a Cu Kα source ($\lambda = 1.54$ Å) and a grazing incidence attachment. The angle of incidence was fixed at 2°. Transmission electron microscopy (TEM) was carried out employing a Philips CM 200-UT microscope (200 kV acceleration voltage). The achieved spot resolution was 0.187 nm and the resolvable offset was 0.11 nm.

The method of instantaneous recording of the electromotive force (the MIE method) was employed in order to follow phase formation and transformation processes of the sputtered

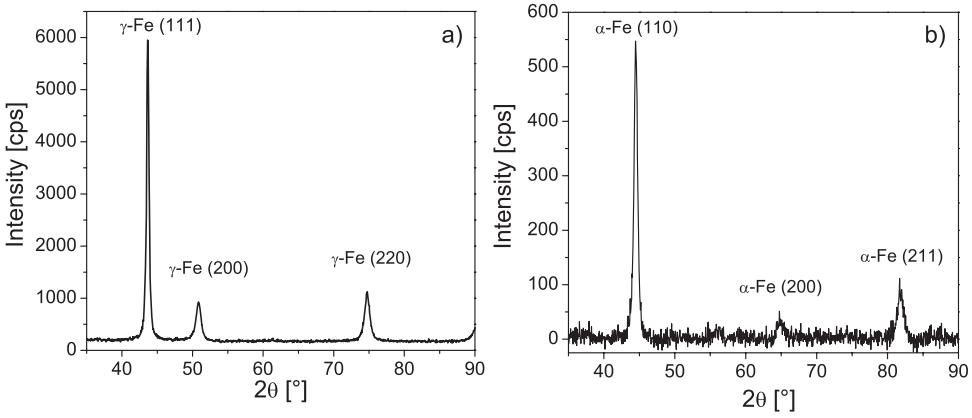

Figure 1. XRD spectra: (a) θ–2θ pattern of the AISI 316 sputter target; (b) GIXRD (2° incidence angle) pattern of the film sputtered from this target at room temperature with a magnetron power of 100 W and an Ar gas flow of 10 sccm. The reflexes of the γ- and α-phases are indexed.

films [17]. The basic setup of this method is the same as that of a galvanic cell with a standard-hydrogen electrode as reference electrode. Pure water was used as the electrolyte.

The magneto-optical Kerr effect (MOKE) was used to investigate the ferromagnetic behaviour of the samples. The measurements were carried out in longitudinal geometry at room temperature, using a polarization-compensator sample analyser (PCSA) ellipsometer and a maximum external magnetic field of 0.15 T. More details can be found in [18]. The samples were mounted on a revolvable holder, so that magnetic anisotropies could be analysed by rotating the sample.

3. Results

3.1. Deposition at room temperature

The x-ray diffraction (XRD) pattern of the starting target material is shown in figure 1(a). The pure γ-phase is easily confirmed. A lattice parameter of $a = 3.592(2)$ Å can be extracted for this fcc structure. After magnetron sputtering from this non-magnetic austenitic stainless steel target (γ) at room temperature, a film exhibiting the α-phase is obtained, as revealed by the XRD pattern shown in figure 1(b). A lattice parameter of $a = 2.876(2)$ Å can be extracted for the bcc structure.

No other reflexes can be clearly seen for the sputtered film; in particular those of the γ-phase are absent. The existence of large amounts of amorphous material can also be excluded from these measurements. A mean grain size of 30(5) nm can be calculated for the (110) reflex with the Scherrer formula [19]

$$\Delta\beta = \frac{0.89\lambda}{d\cos\theta} \tag{1}$$

for the α-phase with the line broadening $\Delta\beta$ for reflexes at a scattering angle θ, assuming the absence of stresses and strains.

MOKE measurements as presented in figure 2 clearly demonstrate the ferromagnetic behaviour of this sputtered austenitic stainless steel film. A coercive field of $H_C \approx 100$ Oe is found. The observed magnetic in-plane anisotropy is less than 5%. This is may be due to some mechanical stresses in the substrate.

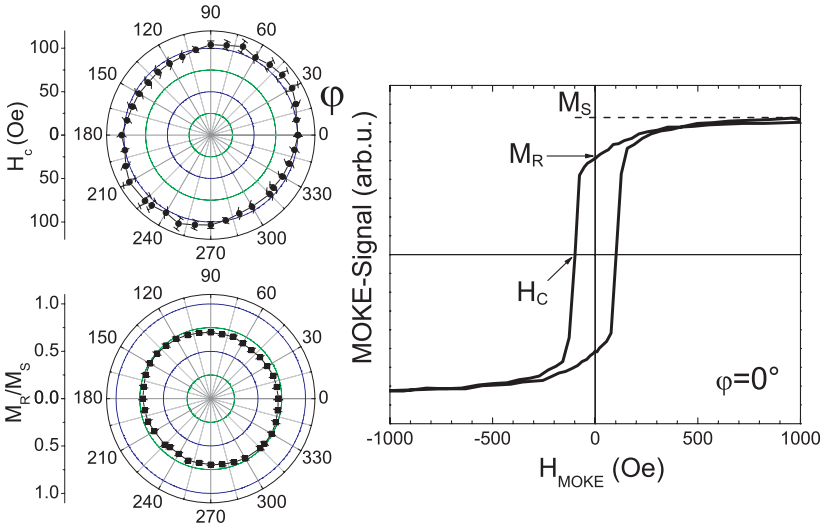

Figure 2. Hysteresis curve of the as-sputtered film in figure 1(b) at $\varphi = 0°$ (right) and polar diagrams of the coercive field H_C and the relative remanence M_R/M_S (left).

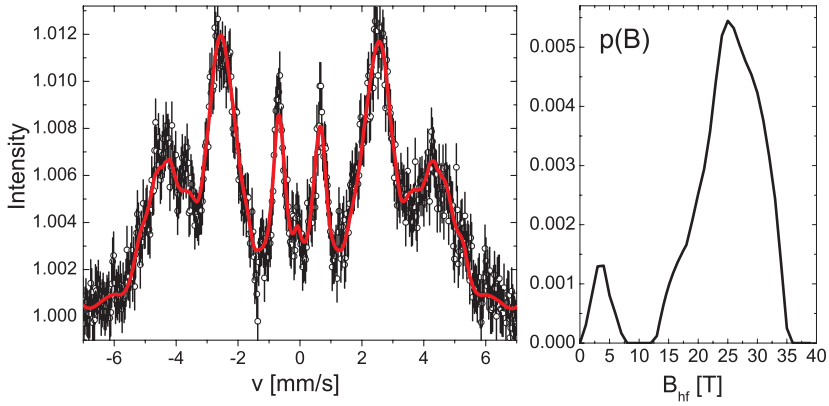

Figure 3. Mössbauer spectrum of the as-sputtered AISI 316 film, deposited at room temperature with 10 sccm Ar gas flow and a magnetron power of 100 W. The hyperfine field distribution $p(B)$ resulting from the numerical analysis is shown on the right-hand side.

Figure 3 shows the Mössbauer spectrum of a sputtered AISI 316 film. It exhibits a broad distribution of magnetically split Zeeman sextets, in accordance with the results of XRD and MOKE. The spectrum clearly indicates that the film is composed of the ferromagnetic α-phase only. The broad distribution shows a similar behaviour to the Mössbauer spectra of amorphous Fe-based alloys; however, due to the fact that the XRD pattern shows the α-phase and does not show an amorphous phase, the broadening is attributed to the variations in the local environment of the Fe atoms, which are surrounded by a varying number of Cr, Ni and Mo neighbours present in the AISI 316 alloy. As described in the literature [11, 20], the hyperfine field B experienced by a given Fe atom depends on the number and distance of Fe and non-Fe neighbouring atoms. For a random bcc structure the probability of having n Fe nearest

neighbours (nn) should follow the binomial distribution

$$P_n = \binom{8}{n} x^n (1-x)^{8-n}, \tag{2}$$

where x is the concentration of Fe (and thus the probability of a given site being occupied by an Fe atom). For AISI 316 we can assume $x = 0.7$. Only configurations (subspectra) with $P_n > 1\%$ were taken into account. This leads to six subspectra, corresponding to the six most probable configurations, represented by the broad distribution of the hyperfine fields as shown in figure 3.

Due to the reduction of the exchange interaction by each non-Fe nn and next-nearest neighbour (nnn) atom, the hyperfine field B decreases for such configurations. This can be represented by the equation

$$B = B_0 - n\Delta B_1 - m\Delta B_2, \tag{3}$$

where n is the number of the non-Fe nn atoms, m the number of non-Fe nnn atoms, ΔH_1 is the hyperfine field reduction by the nn atoms and ΔH_2 the hyperfine field reduction due to the nnn atoms. As known from the literature, the hyperfine field increases linearly with the number of nn atoms. This is also found, for example, for Fe–Al alloys [11]. Each non-Fe nn atom decreases the hyperfine field on average by $\Delta B_1 = 2.4$ T, which is smaller than the values of 2.7–3.2 T reported for Fe–Cr alloys [21, 22]. The smaller decrease in the hyperfine field can be attributed to the presence of Ni and Mo [23, 24] for ferritic stainless steel films. Nevertheless, the hyperfine field with eight nearest neighbours is about 31.3 T. Compared to pure α-Fe this is a decrease of nearly 2 T. In conclusion, this may be due to the influence of the non-Fe nn atoms of the central Fe atoms.

For α-stabilized stainless steel films, each central Fe atom has six nnn atoms. Similar to the analysis above, we can assume that each non-Fe atom decreases the hyperfine field by ΔB_2. As a result of this consideration, $B(8)$ can be written as

$$B(8) = B(8,6) - \Delta B_2 \sum_{m=0}^{6} (6-m) P(8,m) \tag{4}$$

where $B(8,6)$ is the hyperfine field with an eight nn and six nnn configuration, $(6-m)$ the number of the non-Fe nnn atoms, and $P(8,m)$ is the probability for m nnn Fe atoms given by the binomial distribution.

Similar to [11], we estimated the value of $B(8)$ by using the value of $B(8,6)$ of a Fe–Cr alloy; $B(8,6) = 33.5$ T. With this method we obtained a value of $\Delta B_2 = 1.6$ T, which is smaller than $\Delta B_2 = 2.2$ T [21] of Fe–Cr alloys and slightly higher than $\Delta B_2 = 1.2$ T for AISI 304 [11]. As a result of ΔB_1 and ΔB_2 it is reasonable to assume that the effect of non-Fe atoms decreases the hyperfine field with increasing distance of a given Fe atom.

Finally, figure 4 shows a fitted Mössbauer spectrum of the as-sputtered film after hyperfine analysis. Here, M1 represents a subspectrum of a Fe atom with a random neighbourhood consisting of Cr, Ni and Mo atoms. M2 represents the subspectra which can be attributed to the hyperfine parameters of Fe–Cr alloys. The doublet D is most probably the analogue of the small peak in the hyperfine field distribution in figure 3 at very low fields. A small amount of γ-phase can be present here, too. The results of our analysis are summarized in table 1.

The fact that the α-phase is sputtered off the γ-phase target might be due to compositional effects. In fact, a different stoichiometry of the sputtered films is observed after deposition. EDX analysis showed a decrease in the Ni content in the sputtered films. The Ni depletion increased with decreasing gas flow and amounted to 3 at.% at an Ar gas flow of 6 sccm. The loss of Ni content has a strong influence on the phase formation. For AISI 316 a loss of 3 at.%

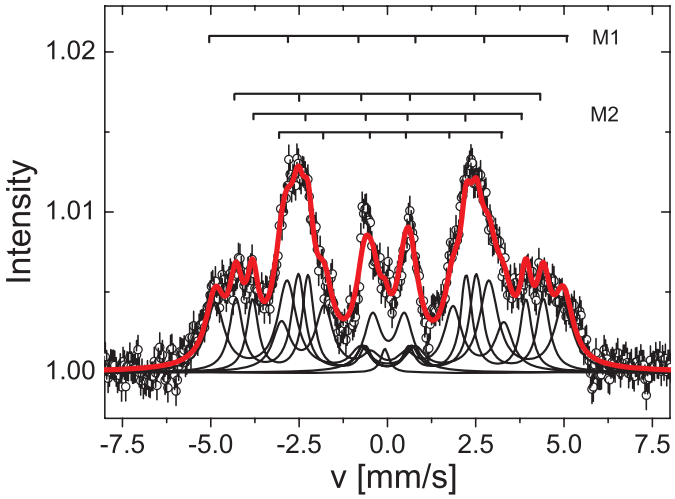

Figure 4. Mössbauer spectrum of the as-sputtered AISI 316 film deposited at room temperature (magnetron power of 100 W; Ar gas flow of 10 sccm) after Lorentzian–Zeeman sextet superposition.

Table 1. Hyperfine interaction parameters of the as-sputtered sample shown in figure 4. Hyperfine parameters: δ is the isomer shift, QS the quadrupole splitting, B the hyperfine field, Γ the line width (FWHM) and RA the relative area.

Subspectra	δ (mm s^{-1})	QS (mm s^{-1})	B (T)	Γ (mm s^{-1})	RA (%)
γ	−0.070(10)			0.300(20)	0.9(12)
D	0.031(49)	0.910(33)		0.574(85)	8.1(21)
M1	0.036(26)	0.021(25)	30.59(30)	0.642(55)	29.5(65)
M2	0.030(20)	0.033(19)	26.98(23)	0.452(53)	22.5(74)
	0.023(19)	0.030(18)	23.99(19)	0.396(44)	19.6(58)
	0.092(39)	0.058(35)	19.52(38)	0.602(65)	19.5(45)

results in a change in its equilibrium state. It changes from austenitic to ferritic, which can be observed in the sputtered films.

The reasons for this depletion in the Ni content are not quite clear. X-ray photoelectron spectroscopy (XPS) for the target showed no evidence of reactive processes during deposition, and the composition of the target was found to be unaltered after several depositions. Therefore it is assumed that this depletion of the Ni content is due to a stronger or faster interaction of Ni with the sputtering plasma or residual oxygen in the chamber. For higher growth rates induced by higher Ar gas flows this depletion becomes less severe.

3.2. Vacuum annealing of room temperature deposited films

Figure 5 shows the Mössbauer spectra obtained for an isochronal annealing series of films sputtered at room temperature. They were vacuum annealed in the temperature range from room temperature to 1073 K. The vacuum was better than 10^{-4} Pa and the annealing time was fixed at 1 h.

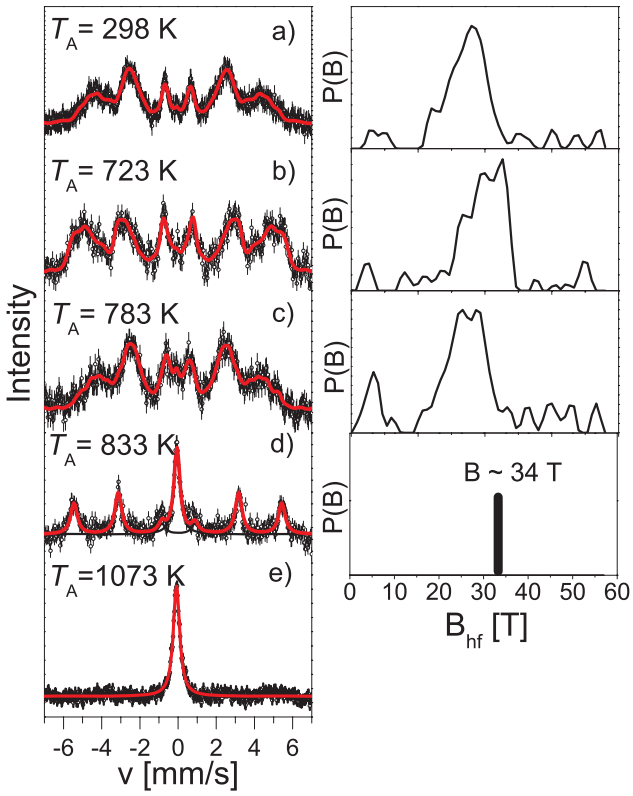

Figure 5. Mössbauer spectra of AISI 316 films sputtered at room temperature (100 W, 10 sccm Ar) after subsequent 1 h annealing in vacuum. The annealing temperatures are given in the graphs. On the right, the hyperfine field distributions of the fits are shown, where appropriate; (d) has no distribution but a well defined field and (e) is purely austenitic.

For lower annealing temperatures one observes changes in the field distribution. The mean field first increases and then decreases again. At the same time, the distribution gets sharper. Interestingly, changes in the intensity ratios are also observed in figure 5(b), where the magnetization is oriented more perpendicular to the film plane. This might be caused by strain in the sample. Upon further annealing, a phase transformation from the α- to the γ-phase takes place between annealing temperatures of 923 and 1023 K. A concurrent EDX analysis of these samples shows an increase in the Ni content with increasing annealing temperature, where finally the film composition is restored to the target stoichiometry. The reason for this is still completely unclear.

These changes in the Ni content are also confirmed by Mössbauer spectroscopy. A recrystallization process advances with increasing annealing temperature and the increasing Ni content can also be observed in the mean hyperfine field, which increases with increasing annealing temperature until the transformation sets in.

This phase transformation is also confirmed by XRD. Up to an annealing temperature of 833 K, a pure α-phase is seen in the diffraction pattern, which changes to a mixture of α- and γ-phases and finally changes rapidly to the pure γ-phase at an annealing temperature of 1073 K. The XRD pattern of the film after this last annealing step is displayed in figure 6. A lattice constant of $a = 3.589(2)$ Å is derived for the observed fcc phase. The XRD pattern shows

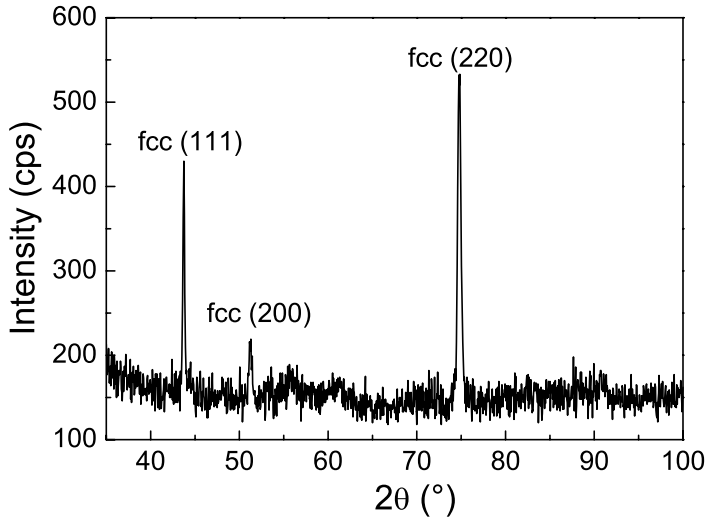

Figure 6. GIXRD (2°) pattern of an AISI 316 film sputtered at room temperature (100 W, 10 sccm Ar) and annealed at 1073 K for 1 h.

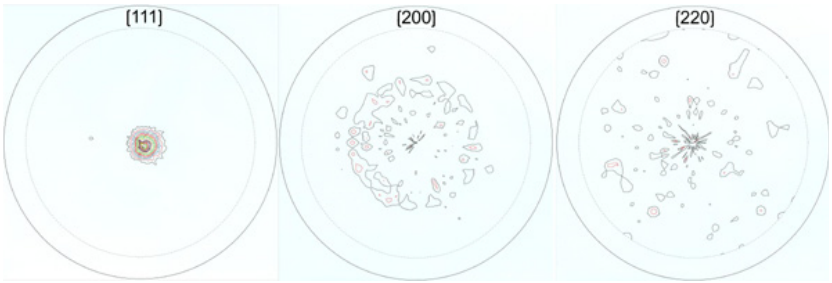

Figure 7. Pole figures of the (111), (200) and (220) reflexes of an AISI 316 film sputtered at room temperature (100 W, 10 sccm Ar) and annealed at 1073 K for 1 h.

a texture, that indicates a preferential orientation of the grains. Consequently, a pole figure measurement was performed, which is displayed in figure 7. From the character and form of the pole figures a (111) texture of the film can be deduced. The (200) and (220) pole figures hint towards a fibre texture [25].

Based on the GIXRD measurements, a stress analysis was carried out [26], showing that in all the samples a stress of 1% of the elastic modulus E is observed. This corresponds to a stress in the film of about 1–2 GPa, which can be identified as tensile stress. This stress—already observed in the magnetic orientation in the Mössbauer spectra—can influence the phase transformation during annealing but also the phase formation during the deposition process. Another hint of a stress-induced phase transformation is given by the misfit of the lattice constants of the α- and γ-phase with their difference in thermal expansion coefficients.

3.2.1. Modelling of the phase transformation during annealing. In order to understand the transformation and recrystallization processes, isothermal annealing experiments were performed. These were then interpreted using the kinetic models of Johnson–Mehl–Avrami (JMA) [27, 28] and Austin–Rickett (AR) [29]. In these models, the transformed fraction C,

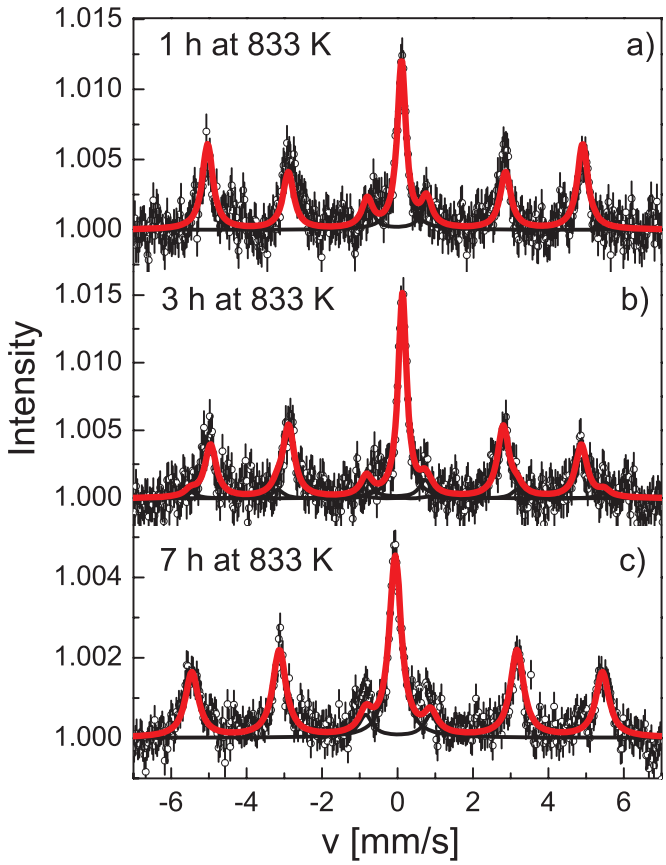

Figure 8. Mössbauer spectra of AISI 316 films sputtered at room temperature (100 W; 10 sccm Ar) after isothermal annealing at 833 K for annealing times of 1, 3 and 7 h.

i.e. the abundance of the γ phase, as obtained from Mössbauer spectroscopy, is a function of time. It is given by the JMA model as:

$$C = 1 - \exp[(-Kt)^n] \tag{5}$$

and by the AR model as:

$$\frac{C}{1-C} = (K't)^m \tag{6}$$

where K and K' are the kinetic constants and n, m the reaction orders (exponents).

The JMA model describes the development of a phase or structure transformation at a constant temperature. By means of equation (5) we obtain a rough crystallization rate. The JMA model describes the complete transformation process by two parameters; the nucleation rate K and the growth velocity n of the newly formed phases. The AR model is an alternative nucleation-growth model, which neglects overlapping volumes during the reaction.

Figure 8 displays the Mössbauer spectra obtained for AISI 316 films after isothermal annealing at 833 K. They exhibit two main components, the first one is a single line due to the (trans-)formed paramagnetic γ-phase and the second are sextets attributed to the remaining ferromagnetic α-phase. The results of the Mössbauer analyses are given in table 2.

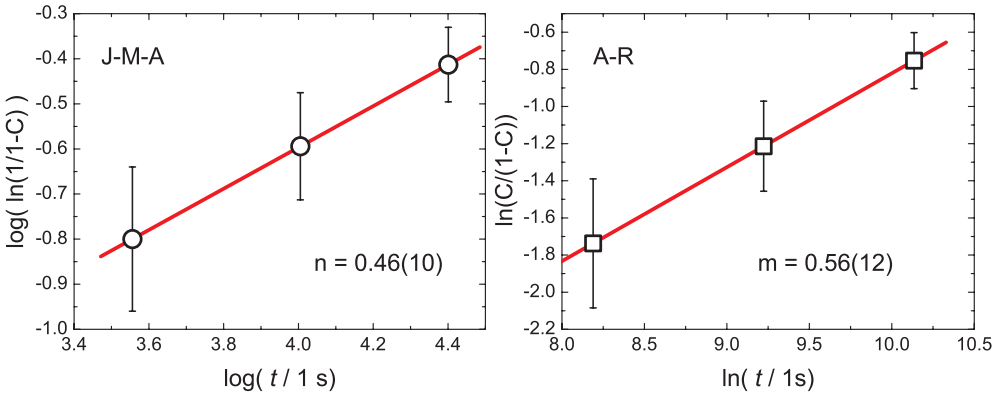

Figure 9. Determination of the reaction exponents for the transformation kinetics according to the JMA and AR models.

Table 2. Results of the Mössbauer analysis of the films after isothermal annealing at 833 K.

Annealing time (h)	Subspectra	δ (mm s^{-1})	QS (mm s^{-1})	B (T)	Γ (mm s^{-1})	RA (%)
1	γ	−0.100(31)			0.566(47)	22.6(32)
	α_a	−0.069(34)	−0.011(33)	31.70(27)	0.758(52)	77.4(11)
	γ	−0.090(19)			0.372(19)	26.8(29)
3	α_a	−0.082(82)	−0.074(82)	30.61(67)	0.400(13)	66.6(86)
	α_b	−0.019(24)	+0.022(24)	33.92(20)	0.394(41)	6.6(21)
7	γ	−0.059(14)			0.384(21)	32.9(25)
	α_b	+0.005(18)	−0.014(18)	33.95(14)	0.424(28)	67.1(77)

The transformed fraction C is easily obtained from the ratio of the central austenite peak area to the total area. Using equation (5) and plotting $\ln[1/(1-C)]$ against t, the JMA kinetic order n can be obtained. Linear regression for the present case yields a JMA exponent of $n = 0.46(12)$. By plotting $\ln[C/(1-C)]$ against $\ln t$, the AR exponent is deduced to be $m = 0.56(10)$.

These results, as presented in figure 9, can now be compared to existing parameters from the literature. Given that the available kinetic parameters are mainly concerned with the JMA exponent, the discussion will focus only on this parameter. Table 3 shows the Avrami exponents for various phase transformations from the literature.

In bulk materials, an Avrami exponent of $n = 1$ is obtained from interface-controlled growth of a phase, i.e. when nucleation occurs at grain boundaries [35]; for thin films lower values can be derived [32]. In accordance with the investigations of Boubeker *et al* [31] and with the TEM results presented below, we suppose that the exponent can be attributed to a reduced dimension growth mechanism, as described in [31, 32]. This growth mechanism has been reported by several authors and is known for bulk materials as well as for thin films. n values between 0.45 and 1.1 are attributed to interface-controlled reactions, dominated by boundary nucleation.

3.2.2. The hyperfine field of the ferromagnetic component. Another characteristic of the Mössbauer spectra is that the local environment of Fe in the alloy changes. With increasing

Table 3. Avrami exponents n for various phase transformations in Fe-based alloys.

n	Study	Proposed process	Refs.
0.3	Isothermally aged bulk steel (GXCr13Ni4)	Stress assisted transformation	[30]
0.53	Transformation in ion-sputtered AISI 304 films	Nucleation at grain boundaries	[31]
0.65	Decomposition of metastable phases in sputter-deposited Fe–Ag	%	[32]
0.45–1.1	η to G transformation in electrodeposited Fe–Zn coatings	Nucleation at grain boundaries	[33]
0.9	Crystallization of amorphous Fe–Cr based alloys	%	[34]

Table 4. Activation energies Q for various diffusion phenomena taken from the literature.

Q (kJ mol^{-1})	Corresponding phenomenon	Ref.
255	Self-diffusion in α-Fe	[37]
284	Self-diffusion in γ-Fe	[37]
309	Self-diffusion in Cr	[37]
280	Self-diffusion in Cr	[37]
251	Cr diffusion in α-Fe	[37]
293	Cr diffusion in γ-Fe	[37]
251–418	Cr diffusion in various SS	[38–42]
297–305	γ- to α-phase transformation in 9Cr1Mo bulk steel	[43]

annealing time a separation of the ferromagnetic components is observed and can be attributed to the presence of two inequivalent ferromagnetic Fe sites in the film. It seems that regions with higher concentrations of Ni have transformed into the γ-phase, thus leaving an α-phase with a lower content of alloying elements and giving rise to a increase in the hyperfine field to 33 T. Thus it can be assumed that the Cr diffuses out of the grains and is used to form Cr-carbides. This phenomenon is known in bulk material [36]. Due to the experimental uncertainties in the subspectral areas, we were not able to correlate the transformed area to the area of the remaining α-phase.

3.2.3. Arrhenius law and activation energy Q. The kinetic constant K in the JMA law as given in equation (5) follows the Arrhenius law according to

$$K = K_0 \exp(-Q/RT) \tag{7}$$

where K_0 is the pre-exponential factor, Q the activation energy, R the universal gas constant and T the absolute temperature. In order to derive the value of Q, additional isochronal annealing series were done at annealing temperatures of 783, 833 and 923 K and subsequently analysed. The annealing time was fixed at 1 h. Again the transformed fraction C was deduced from the Mössbauer spectra. The Arrhenius plot is shown in figure 10 and its analysis results in an activation energy of 377.55(80) kJ mol^{-1}.

In order to interpret this activation energy, a comparison with the values given in the literature is inevitable. Table 4 summarizes the activation energy values for phase transformations in Fe-based disordered systems, especially for amorphous to crystalline transformations in metallic glasses.

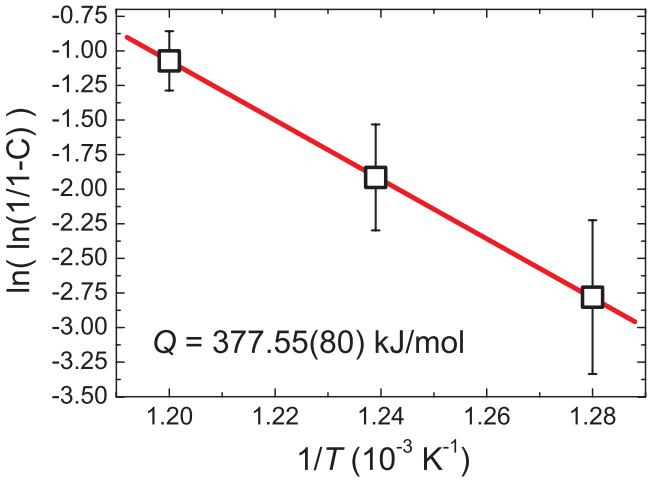

Figure 10. Determination of the activation energy Q within the Johnson–Mehl–Avrami model deduced by isochronal annealing experiments (for 1 h).

The activation energy of 377.55(80) kJ mol^{-1} derived from the presented experiments is somewhat higher than the energies for lattice self-diffusion of Fe, Cr and Ni, but it is in agreement with the value given for Cr substitutional diffusion in austenitic steel [38–42]. Finally, it is worth mentioning that getting a diffusion coefficient out of kinetics data is only an approximation when more than one mechanism occurs, i.e. here Cr-carbide precipitation and a phase transformation from the α- to the γ-phase.

3.3. The influence of the deposition temperature

Figure 11 shows the Mössbauer spectra of AISI 316 films deposited at increasing substrate temperatures. A sudden phase transformation from the α- to the γ-phase was observed between deposition temperatures of 723 and 768 K. In addition, the relative line intensities of the sextets change significantly. For a Mössbauer Zeeman sextet, the relative line intensities between the second (fifth) and first (sixth) peak can be written as:

$$\frac{A_{2,5}}{A_{1,6}} = \frac{4\sin^2\theta}{3(1+\cos^2\theta)} \tag{8}$$

where θ is the angle between the γ-ray direction and the magnetization direction [14, 44]. For the AISI 316 film sputtered at room temperature, the ratio $A_{2,5}/A_{1,6}$ is 0.83(2), which deviates slightly from that of the random orientation of the magnetic moments (0.666). This implies that the orientation of the average magnetic moments inclines to be in the in-plane direction, which is normal for thin films. For higher deposition temperatures, the ratio decreases. The ratio amounts to 0.27(3) for the film sputtered at 723 K. Hence, a rotation of the average magnetic moments to the out-of-plane direction has taken place. For α-Fe in bulk materials, easy magnetization is in the [100] direction, but it seems that the easy magnetization direction for sputtered AISI 316 films could be dominated by geometrical demagnetization effects, micro-stresses and a possible directional growth. Here, the increasing deposition temperature seems to lead to a stress-release process which induces an out-of-plane magnetization direction. As will be shown later in the TEM pictures, the micro-stress is dominant in as-sputtered AISI 316 films.

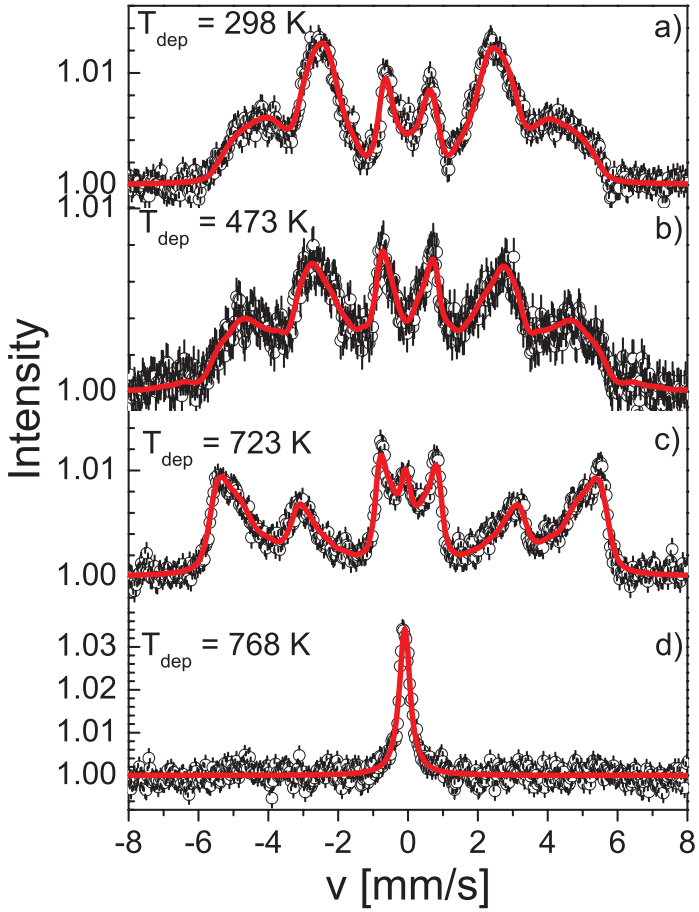

Figure 11. Mössbauer spectra of as-sputtered AISI 316 films deposited at a magnetron power of 100 W and an Ar flow of 10 sccm at various deposition temperatures: (a) room temperature, (b) 473 K, (c) 723 K and (d) 768 K.

Figure 12 shows the XRD pattern of the samples sputtered at 723 and 768 K. The XRD pattern of the as-sputtered sample looks like the pattern of the sample sputtered at 723 K. The pattern of the sample sputtered at 768 K is conspicuous. In contrast to the XRD pattern, the Mössbauer spectrum shows only the γ-phase. The XRD pattern exhibits both, the α-phase ($a = 2.87(1)$ Å) and the γ-phase ($a = 3.59(1)$ Å). This can be explained by the different information depths of these methods. CEMS has an information depth of about 150 nm, whereas GIXRD with $\omega = 2°$ corresponds to an information depth of approximately 350 nm. This is then a hint that this sample consists of a bilayer system in which the α-phase is primarily built at the beginning of the deposition process. During the course of the deposition, and with increasing film thickness, the γ-phase becomes thermodynamically favoured. It is important to mention that the phase transformation in this case is not induced by compositional effects. The Ni content is identical in both samples and below the γ-phase stabilizing limit of 8%, which means that another mechanism has to be found to explain the different phase formation observed in these films.

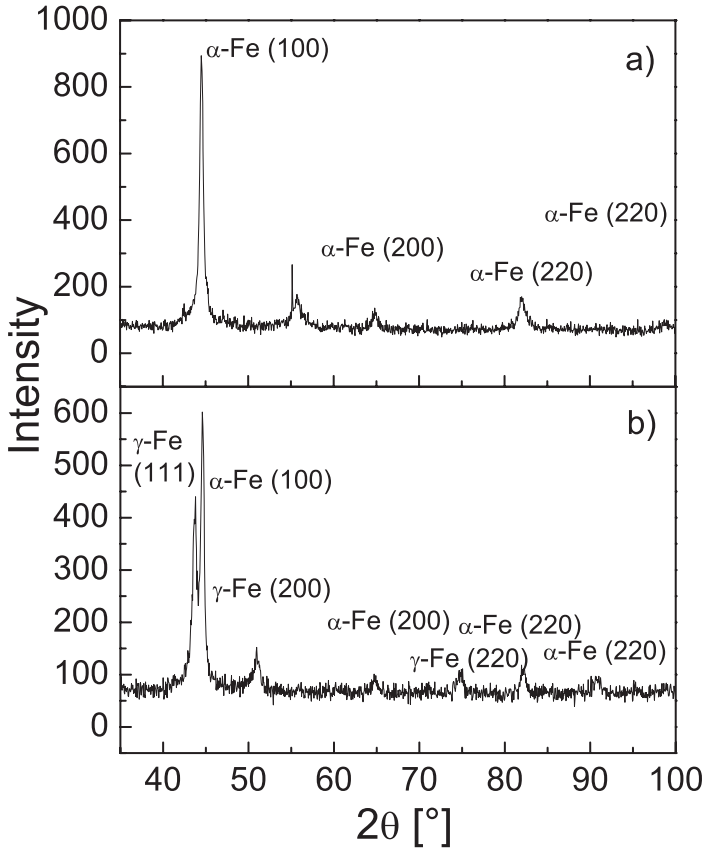

Figure 12. GIXRD pattern of AISI 316 films sputtered with a magnetron power of 100 W and 10 sccm Ar flow at deposition temperatures of (a) 723 K and (b) 768 K.

3.4. MIE and the Gibbs–Thomson effect

In order to reach a better understanding of the phase formation in the sputtered stainless steel films, electrochemical experiments were carried out. The MIE method can be used to investigate the phase formation process in the sputtered films. From the results of the previous experiments, the temperature was found to be a crucial factor for phase formation. These results also indicate that here the Ni content could play a role too.

MIE was used to determine the Gibbs free energy ΔG by the equation

$$\Delta G = -zF\Delta E, \tag{9}$$

where z represent the number of transferred electrons during the reaction, F is the Faraday constant and ΔE is the deviation of the cathode and anode potential. Equation (9) is equivalent to the Gibbs–Duhem relation. This allowed us to re-evaluate and re-interpret the ΔG by two methods, namely,

(i) by the variation of the chemical potential of Ni $\Delta\mu_{\mathrm{Ni}}$ with the Ni content x described by the Gibbs–Duhem relation (equation (9), i.e. measured by MIE)

$$\Delta G = (1-x)\int_0^{\frac{x}{1-x}} \Delta\mu_{\mathrm{Ni}}\,\mathrm{d}\left(\frac{x}{1-x}\right); \tag{10}$$

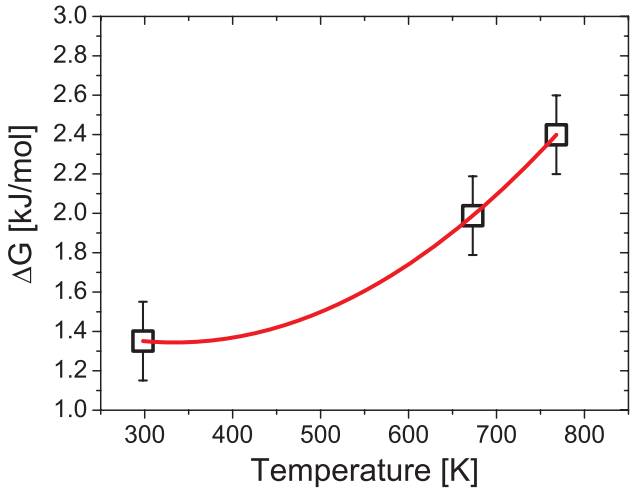

Figure 13. Evolution of the measured Gibbs free energy of the sputtered samples with increasing substrate temperature. The fit corresponds to a parabola which is used to determine the minimum of the Gibbs free energy of the system.

Table 5. Measured and calculated ΔG determined by methods (i) and (ii).

T (K)	$\Delta G_{(i)}$ (kJ mol^{-1})	$\Delta G_{(ii)}$ (kJ mol^{-1})
298	1.351(5)	1.213(2)
723	1.988(5)	1.838(3)
768	2.399(5)	2.311(2)

(ii) by using data for $\Delta\mu_i$ (i = Fe, Cr, Ni and Mo) with the relation described in [45].

Figure 13 shows the values of ΔG for sputtered samples with increasing substrate temperature as obtained from MIE. Table 5 compares the values of ΔG determined by the two previously mentioned methods for sputtered samples with increasing substrate temperature.

The data by method (i) overlap nicely with those calculated by the theoretical model (ii). This indicates that the chemical potential $\Delta\mu_{\mathrm{Ni}}$ dominates the Gibbs free energy of the sputtered samples. Consequently, the hint that Ni represents a critical factor for formation of phase stability is confirmed. Now, we have to explain the behaviour of ΔG, i.e. we need a model which can explain the steady rise of the Gibbs free energy. Sarkar *et al* [46] discuss in their work the Gibbs–Thomson effect in Fe–Ge, and in our opinion this could explain the steady rise of ΔG. The Gibbs–Thomson relation is given by

$$\Delta G = 2\sigma_{\mathrm{S}} V_{\mathrm{m}} / R_{\mathrm{G}}, \tag{11}$$

where σ_{S} represents the surface energy, V_{m} is the molar volume and is R_{G} the radius of the grains. Thus it appears that the surface energy and the radius of the grains are the important parameters for phase formation. In the case of increasing substrate temperature, the Gibbs–Thomson effect could explain the phase transformation as follows: to explain the higher ΔG, the surface energy σ_{S} has to increase, which has to result in smaller grain sizes. But more energy is needed to maximize the surface energy. This energy is extracted from the kinetic energy as a result of the increasing temperature. By this consideration, we have to find smaller grain sizes with increasing temperature if the Gibbs–Thomson effect is a suitable model for explaining the

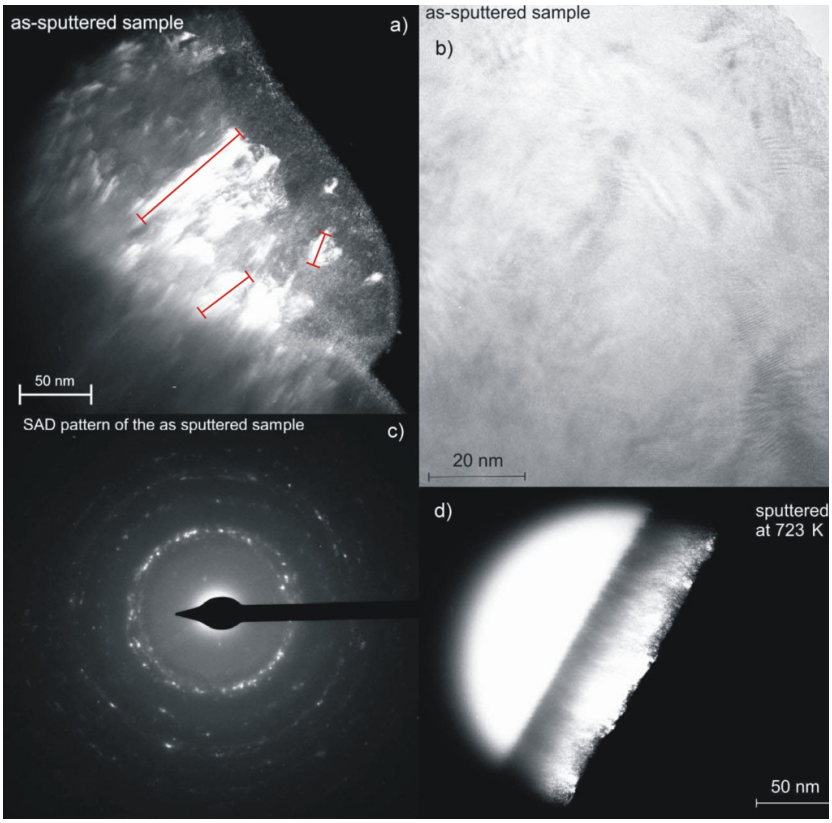

Figure 14. TEM results for deposited stainless steel films: (a) dark field TEM picture of AISI 316 film sputtered at room temperature (100 W, 10 sccm Ar), some grains for size determination are indicated; (b) bright field picture of film shown in (a); (c) selected area diffraction (SAD) pattern of the film shown in (a); (d) dark field TEM picture of an AISI 316 film deposited at 723 K.

observed dependences. Indeed this dependence is found by the TEM investigations shown in figure 14.

As a result of the TEM investigation, the grain sizes are found to decrease from 30–80 nm at room temperature to 5–10 nm at 723 K. The observed grain sizes were determined by means of the magnification factor marked with the lines in figure 14(a). This confirms the predictions of the Gibbs–Thomson effect. Furthermore, the reduced dimension growth mechanism can be seen in figure 14: at room temperature we observe a coherent film with a primary layer accretion, but the coherence gets lost at higher temperatures. The moiré-figures in figure 14(b) are conspicuous. These indicate micro-stresses, which could influence the spin orientation (this was already observed in the line ratios in the Mössbauer spectra). The SAD pattern of the as-sputtered film deposited at room temperature shows that these micro-stresses are a result of the mixing of phases in the film. Because of the overlapping diffraction rings we were not able to calculate the lattice constants.

In the case of vacuum annealing, the Gibbs–Thomson effect is also able to explain the observed phase transformation. From the JMA kinetic investigation we conclude that Cr diffuses out of the grains to form Cr-carbides. This results in a change of the stoichiometry of the film which is confirmed by EDX; the Ni content increased with increasing annealing

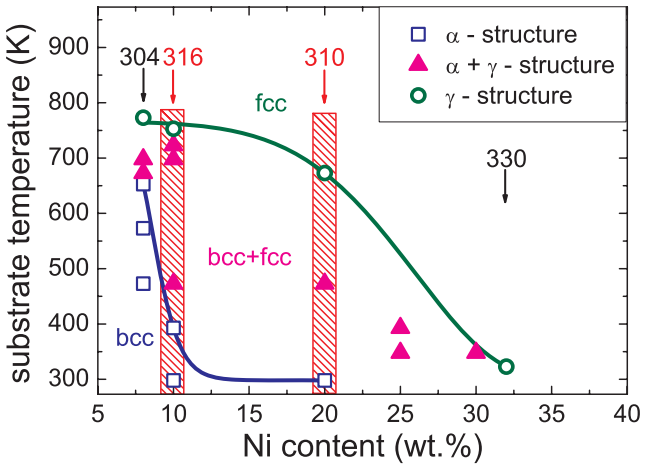

Figure 15. *Sputter diagram* for magnetron sputtering of austenitic stainless steel. The numbers represent the AISI steel grade. The hatched boxes indicate the two steel grades and the data from this study and unpublished data [48]. The lines hint at the phase borders.

temperature. Another consequence of the Cr diffusion is an enlargement of the grain size [12]. The Gibbs–Thomson effect would now predict a lower Gibbs free energy. However, from thermodynamic calculations [47], the higher Ni content in association with the higher temperature is able to stabilize the γ-phase. Consequently, we can assume that the Gibbs–Thomson effect is able to explain phase transformations in austenitic stainless steel films. The force of this phenomenon is assumed to be the variation of surface Gibbs free energy as a function of the grain size in the different phases. As a summary of this study, we added our data together with data from the literature [4, 9, 10, 12]. This leads to a 'sputter diagram' for magnetron sputtering of austenitic stainless steel as given in figure 15. It seems that besides the temperature, the stoichiometry, in particular the Ni content, is also a dominating factor for phase formation in sputtered stainless steel films. This *phase diagram* shows an empirical plot of phases (and not a regular phase diagram) observed in sputtered stainless steel films as a function of the temperature during deposition and the Ni content of the target. The lines drawn in figure 15 show the possible phase boundary that separates three phase regions: the α-phase region, mixture of the α- and γ-phase, and a γ-phase region. The boxes show the data from this study and unpublished data where we also studied the behaviour of sputtered AISI 310 films. For test purposes we made AISI 316 films by pulsed laser deposition (PLD) and we discovered that this diagram is also applicable to other deposition techniques.

4. Conclusions

Various aspects of the phase formation and stability in magnetron sputtered austenitic stainless steel films were studied.

The magnetic properties investigated by means of Mössbauer spectroscopy and MOKE showed that the alloying elements (Cr, Ni and Mo) have a clear influence on the local magnetic properties, whose magnitudes are closely related to the number and distance of the neighbouring atoms. We found that each non-Fe atom decreases the hyperfine field by about 2.4 T, and each next-nearest neighbour atom by about 1.6 T, in accordance with published data.

Vacuum-annealed samples showed a phase transformation from bcc to fcc between annealing temperatures of 923 and 1023 K. This phase transformation could be described

by the kinetic models of Johnson–Mehl–Avrami and Austin–Rickett. We found a JMA exponent of $n = 0.46(10)$ and an AR exponent of $m = 0.56(12)$. An activation energy of 377.55(80) kJ mol^{-1} was deduced from the Arrhenius law and a comparison with the literature showed that Cr diffuses out of the grains, probably to form mixed Cr-carbides.

Increasing the deposition temperature leads to a phase transformation between 723 and 768 K. While the initiation phenomena are different, the phase transformations can be explained with the Gibbs–Thomson effect, where the Gibbs free energy is described by a variation of grain size in different phases. These microstructural features were investigated and confirmed by TEM. With an accurate EDX composition analysis Ni depletion was observed in the sputtered films with respect to the sputtering target. This was confirmed by MIE experiments which showed that the Gibbs free energy of sputtered AISI 316 films is dominated by the chemical potential $\Delta\mu$ of Ni. As a consequence of these experiments, we found the deposition temperature and the Ni content to be the dominating factors for phase formation and stability. This was summarized in a sputter phase diagram.

Acknowledgments

We would like to thank Professor Dr Jörg Schröder and Heike Rohmann from the Institute of Physical Chemistry, Göttingen for their support with the MIE experiments and discussions about the results.

References

[1] Eymery J P and Laplanche G 1991 *J. Magn. Magn. Mater.* **93** 179–82
[2] Eymery J P, Laplanche G, Cahoreau M and Denanot M F 1992 *Thin Solid Films* **217** 1–6
[3] Boubeker B, Goudeau P, Serrari A and Eymery J P 1999 *Nucl. Instrum. Methods Phys. Res.* B **155** 289–94
[4] Godbole M J, Pedraza A J, Allard L F and Geesey G 1992 *J. Mater. Sci.* **27** 5585–90
[5] Godbole M J, Pedraza A J, Park J W and Geesey G 1993 *Scr. Metall. Mater.* **28** 1201–6
[6] Inoue S, Saeki T, Uchida H, Koterazawa K and Iwasa M 2002 *Vacuum* **66** 257–61
[7] Koskinen J, Torri P, Hirvonen J P, Mahiout A and Stanishevsky A 1996 *Surf. Coat. Technol.* **80** 57–60
[8] Eymery J P, Merakeb N, Goudeau P, Fnidiki A and Bouzabata B 2003 *J. Magn. Magn. Mater.* **256** 227–36
[9] Dahlgren S D 1970 *Metall. Trans.* **1** 3095
[10] Malavasi S, Oueldennaoua A, Foos M and Frantz C 1987 *J. Vac. Sci. Technol.* A **5** 1888–91
[11] Li F S, Sun J J and Chien C L 1995 *J. Phys.: Condens. Matter* **7** 1921–31
[12] Zhang X, Misra A, Schulze R K, Wetteland C J, Wang H and Nastasi M 2004 *J. Mater. Res.* **19** 1696–702
[13] Schaaf P and Gonser U 1990 *Hyperfine Interact.* **57** 2101–4
[14] Schaaf P 2002 *Prog. Mater. Sci.* **47** 1–161
[15] Brand R A 1992 *NORMOS—Mössbauer Fitting Program*
[16] Landry F and Schaaf P 1996 WinISO fit program for Mössbauer spectra, unpublished
[17] Rostovtsev R N 2002 *Met. Sci. Heat Treatment* **44** 211–3
[18] Müller G A 2004 Ion-beam induced changes of magnetic and structural properties in thin Fe films *PhD Thesis* University of Göttingen
[19] Scherrer P 1918 *Nachr. Ges. Wiss. Gött.* **2** 98–100
[20] Czjzek G and Berger W G 1970 *Phys. Rev.* B **1** 957
[21] Dubiel S M and Zukrowski J 1981 *J. Magn. Magn. Mater.* **23** 214–28
[22] Schaaf P, Bauer P and Gonser U 1989 *Z. Metallk.* **80** 77–82
[23] Vincze I and Campbell I A 1973 *J. Phys. F: Met. Phys.* **3** 647–63
[24] Marcus H L and Schwartz L H 1967 *Phys. Rev.* **162** 259
[25] Knorr D B and Livingston J D 1989 *Supercond. Sci. Technol.* **1** 302–6
[26] Carpene E 2002 Excimer laser treatments of iron, aluminum, and silicon in nitrogen and methane atmosphere *PhD Thesis* University of Göttingen
[27] Johnson W A and Mehl R F 1939 *Trans. Metall. Soc. AIME* **135** 416–59
[28] Avrami M 1939 *J. Chem. Phys.* **7** 1103–12

[29] Austin J B and Rickett R L 1939 *Trans. Metall. Soc. AIME* **135** 396–415
[30] Kuzmann E, Varga I and Vertes A 1993 *Nucl. Instrum. Methods Phys. Res.* B **76** 292–4
[31] Boubeker B, Eymery J P, Auric P and Rahmoune M 1995 *Nucl. Instrum. Methods Phys. Res.* B **101** 267–74
[32] Kataoka N, Sumiyama K and Nakamura Y 1989 *Acta Metall. Mater.* **37** 1135–42
[33] Drewien C A, Goldstein J I and Marder A R 1994 *Metall. Mater. Trans.* A **25** 1119–25
[34] Kadiri H, Djegamariadassou C, Rougier P, Dormann J L, Berrada A and Renaudin P 1988 *J. Physique Coll.* **49** C 8 1371–2
[35] Cahn R W and Haasen P 1983 *Physical Metallurgy* 3rd edn (Amsterdam: North-Holland Physics Publishing)
[36] Ortner S R 1991 *Acta Metall. Mater.* **39** 341–50
[37] Smithells C J 1976 *Metals Reference Book* 6th edn (London: Butterworths)
[38] Thorvaldsson T and Salwen A 1984 *Scr. Metall.* **18** 739–42
[39] Linnenbom V, Tetenbaum M and Cheek C 1955 *J. Appl. Phys.* **26** 932–6
[40] Ganesan V, Seetharaman V and Raghunathan V S 1983 *J. Nucl. Mater.* **118** 313–9
[41] Daruvala H S and Bube K R 1979 *Mater. Sci. Eng.* **41** 293–5
[42] Jenkins C F and Smith G V 1969 *Trans. Metall. Soc. AIME* **245** 2149
[43] Brachet J C 1991 *PhD Thesis* University of Paris-Sud
[44] Schaaf P 2005 Mössbauer spectroscopy *Encyclopedia of Condensed Matter Physics* vol 4, ed G Bassani, G Liedl and P Wyder (Oxford: Elsevier-Associated Press) pp 20–31
[45] Hillert M and Waldenstrom M 1977 *Scand. J. Metall.* **6** 211–8
[46] Sarkar S, Bansal C and Chatterjee A 2000 *Phys. Rev.* B **62** 3218–22
[47] Du H 1993 *J. Phase Equilib.* **14** 682–93
[48] Cusenza S and Schaaf P 2007 Magnetron sputtering of AISI 310 austenitic stainless steel films, unpublished